Peer-reviewed version available at *Ceramics* **2020**, *3*, 171-188; doi:10.3390/ceramics3020016

Article

Transient Thermo-mechanical Analysis of Steel Ladle Refractory Linings using Mechanical Homogenization Approach

Mahmoud Ali [1], Thomas Sayet [1], Alain Gasser [1], Eric Blond [1]

[1] Univ. Orléans, Univ. Tours, INSA-CVL, LaMé (EA 7494), 8 rue Léonard de Vinci, 45072 Orléans, France
mahmoud.ali@univ-orleans.fr (M.A), thomas.sayet@univ-orleans.fr (T.S), alain.gasser@univ-orleans.fr (A.G), eric.blond@univ-orleans.fr (E.B)
* Correspondence: (M.A and A.G)

Abstract: Mortarless refractory masonry structures are widely used in the steel industry for the linings of many high-temperature industrial applications including steel ladle. The design and the optimization of these components require accurate numerical models that consider the presence of joints as well as joints closure and opening due to cyclic heating and cooling. The present work reports on the formulation, numerical implementation, validation, and application of homogenized numerical models for simulation of refractory masonry structures with dry joints. The validated constitutive model has been used to simulate a steel ladle and to analyze its transient thermomechanical behavior during a typical thermal cycle of steel ladle. 3D solution domain, enhanced thermal and mechanical boundary conditions have been used. Parametric studies to investigate the impact of joints thickness on the thermomechanical response of the ladle have been carried out. The results clearly demonstrate that the thermomechanical behavior of mortarless masonry is orthotropic nonlinear due to gradual closure and reopening of joints with the increase and decrease of temperature. Also, resulting thermal stresses increase with the increase of temperature and decrease with the increase of joints thickness.

Keywords: Refractories; Mortarless Masonry; Mechanical Homogenization; Thermomechanical Modeling; Steel Ladle.

1. Introduction

Steel ladles are industrial vessels that are used in the steel industry for liquid steel transportation and refinement. Normal operating conditions of steel ladles include high operating temperatures (around $1700°C$), high thermal stresses, slag corrosion and degradation of layers in contact with liquid steel. To withstand these severe operating conditions, steel ladles design is based on the concept of multi-layer design. Each layer has unique thermal, mechanical, physical and chemical properties. The most critical layer in the steel ladle is the working lining layer in contact with liquid steel. As its temperature values are the highest within the ladle. In addition, this layer is usually subjected to thermal shock and severe chemical environment leading to thermomechanical degradation [1].

Generally, working linings are made of refractory masonry bricks separated by small gaps (also called dry joints). Often, these gaps are resulting from the surface roughness of the bricks, brick dimensions and shape errors during manufacturing. But sometimes, for instance in blast furnaces, the initial gaps are designed and obtained using cardboard blocks during the installation of masonry to compensate thermal expansion effects. Indeed, many studies have shown that joints have a great impact on the overall thermomechanical response of mortarless refractory masonry (working lining)

[2,3] as, they allow the bricks to expand freely (until closure of joints) resulting in lower values of compressive stresses then, after closure of joints, compressive stresses increase at a higher rate [4,5].

The design and optimization of steel ladles require accurate thermal and mechanical numerical models with proper boundary conditions and solution domains. Most of previous studies typically focused on studying thermal and heat transfer behavior of steel ladles during steel making process. For instance, Xia and Ahokainen [6] analyzed numerically the impact of preheating temperature and slag heat losses on the thermal stratification in the steel ladle during the holding step. Similarly, Glaser et al. [7] developed a 2D axisymmetric numerical model to investigate heat transfer behavior and heat losses during liquid steel teeming step. Recently, Santos et al. [8] presented a 2D axisymmetric transient thermal numerical model to investigate the impact of lining design on the transient thermal behavior and energy consumption of a steel ladle during preheating, holding liquid steel and being empty.

With regard to thermomechanical modelling of steel ladles, few studies have been carried out. Considering all the bricks and joints of the working lining as well as contact between them leads to increase the computational time and cost. Furthermore, the converged solution (accurate solution) of the computations is not guaranteed. For these reasons, a number of authors have neglected the presence of joints [9], while others considered only few bricks and joints between them [10]. For example, Yilmaz used a 2D steady-state axisymmetric finite element simulation to investigate the thermomechanical response of the ladle. The presence of joints within the working lining and bottom has been neglected and all lining layers have been considered isotropic. Aidong et al. [10] investigated the influence of material properties and linings thickness on the thermomechanical behavior of the slag zone using 2D transient finite element analysis of a few bricks in the slag line zone and Taguchi method. Due to the selected 2D solution domain, only one head joint with 0.4 mm thickness has been considered while bed joints have been neglected.

A reasonable approach to consider the presence of joints and their impact on the thermomechanical response of mortarless masonry without increasing computation costs is to replace the bricks and joints by an equivalent material. Nguyen et al. [4] developed and validated a homogeneous equivalent material model of mortarless refractory masonry structure. This model is based on four joint patterns as well as transition criteria between them. The model considers the influence of joints closure on the thermomechanical response. Gasser et al. [11] used this model and developed a steady-state 3D finite element models of a steel ladle to investigate the influence of bottom design (radial, parallel and fishbone designs) and joints thickness on the resulting thermomechanical stresses. Joints in the ladle bottom have been considered, whereas, joints in the ladle wall have not been taken into account. Their results indicate that using radial design of the ladle bottom results in lower values of von Mises stress in the steel shell as compared to parallel and fish bone designs. Also, Von Mises stresses in the steel shell decrease with the increase of joints thickness.

Previous work on modelling of steel ladles focused on steady state thermomechanical behavior of steel ladles and do not show the transient thermomechanical behavior during a complete thermal cycle of steel making process. The present work is a continuation of previous work presented by Gasser et al. [11] on thermomechanical modelling of steel ladles. The main objective of the present study is to investigate the thermomechanical response of a steel ladle during complete thermal cycles of steel making process. 3D transient thermomechanical analysis of a steel ladle has been performed. An equivalent material model of mortarless masonry structures has been developed, validated, and then used to replace the working linings of a steel ladle. The equivalent material model takes into account the presence of joints as well as joints closure and reopening. The influence of temperature fluctuations and joints thickness on the transient thermomechanical response of the steel ladle have been presented.

The paper is organized as follows: the physical model, materials, thermal and mechanical boundary conditions of the steel ladle thermomechanical model are described in section 2. Development of an equivalent homogenized material model for mortarless masonry structures is given in section 3. In section 4, validation of the developed equivalent material model, temperature

distributions, stress fields in steel ladle are presented and discussed. Conclusion, future work and key findings of the present study are given in section 5.

2. Thermo-mechanical modeling of a steel ladle

2.1. Physical model and materials

Refractories are the best candidate materials for steel ladle application due to their low thermal conductivity, thermal, chemical and mechanical stability at high temperatures. To meet the mechanical, thermal and operational requirements, different refractory layers are used for the construction of the ladle. Each layer has a specific purpose and has unique thermophysical and mechanical properties. The different layers are working lining, safety lining (also called permanent lining) and steel shell (see Fig. 1). The working lining is made of mortarless refractory masonry. The safety lining is composed of two layers: a dense refractory masonry with mortar joints layer with low thermal conductivity and a porous layer with lower thermal conductivity. The mechanical and thermophysical properties of each layer are reported in table 1 where ρ is the density, C_p is the specific heat, k is the thermal conductivity, Y is the Youngs modulus and CTE is the coefficient of thermal expansion.

Table 1. Thermophysical properties of materials used in the present study.

Lining	Zone	Properties		Ref.
Steel shell	Steel shell	ρ (kg/m³)	7840	[8,10]
		k (W/m. K)	47.3 at 200 ^oC 42.3 at 350 ^oC 37.3 at 500 ^oC	
		C_p (J/kg. K)	530 at 200 ^oC	
		Y (GPa)	210 at 20^oC 170 at 400 ^oC	
		CTE ($10^{-6}K^{-1}$)	12	
Safety lining	Bottom & wall bricks (dense layer)	ρ (kg/m³)	2660	[12]
		k (W/m. K)	2.6 at 400 ^oC 2.1 at 800 ^oC 2 at 1200 ^oC	
		C_p (J/kg. K)	1144 at 1200 ^oC	
		Y (GPa)	45	
		CTE ($10^{-6}K^{-1}$)	6	
	Bottom & wall Insulation (porous layer)	ρ (kg/m³)	510	[8,10]
		k (W/m. K)	0.15 at 250 ^oC 0.25 at 800 ^oC 0.34 at 1350 ^oC	
		C_p (J/kg. K)	1047	
		Y (GPa)	0.3	
		CTE ($10^{-6}K^{-1}$)	9	
Working lining	Bottom & wall	ρ (kg/m³)	3210	[10,13,14]
		k (W/m. K)	4.65 at 400 ^oC 3.49 at 700 ^oC	

Preprints (www.preprints.org) | NOT PEER-REVIEWED | Posted: 20 March 2020 doi:10.20944/preprints202003.0305.v1

Peer-reviewed version available at Ceramics 2020, 3, 171-188; doi:10.3390/ceramics3020016

			4.65 at $1000\ ^oC$ 5.81 at $1300\ ^oC$	
		C_p (J/kg. K)	1090	
		Y (GPa)	35 at $20\ ^oC$ 37 at $1000\ ^oC$ 38 at $1500\ ^oC$	
		CTE ($10^{-6}K^{-1}$)	11	

A typical industrial scale steel ladle has complex geometry and is composed of refractory linings, steel construction components, valves, purging plugs, lifting point, etc. In order to reduce the computation time and since the main aim of the present work is to analyze the thermomechanical behavior of the refractory linings, some detailed features such as valves, nozzles and purging plugs have been neglected. Also, due to symmetry, one quarter of the steel ladle has been considered. The simplified physical model of the studied steel ladle is presented in Fig. 1. The height and diameter of the ladle are 5 and $4.6\,m$ respectively. The thickness of each layer is given in mm and reported in Fig. 1.

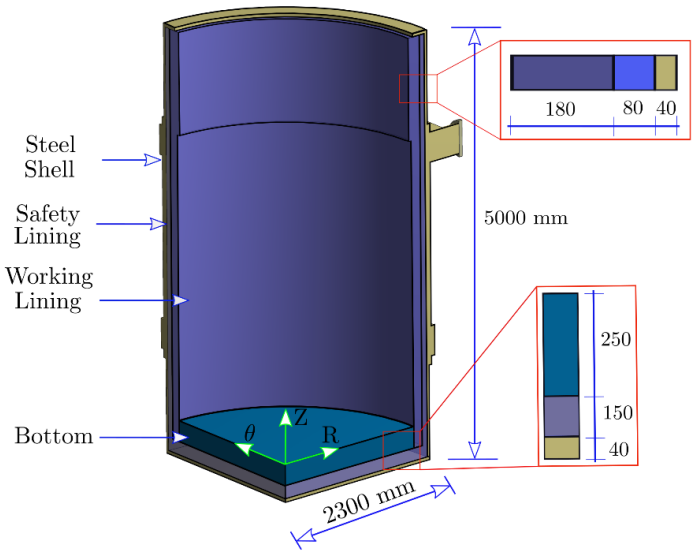

Figure 1. Schematic of a steel ladle showing the different zones and linings.

2.2. *Process description*

In the steel industry, steel ladles are used to transport liquid steel from electric arc furnace or converter to continuous casting machines. Also, they are used as refining units. While holding liquid steel other processes occur in parallel such as degassing and alloying. During this process, the ladle is exposed to different thermal and mechanical operating conditions. A typical thermal cycle of steel ladle refractory linings includes: step 1, preheating the working lining using natural gas burner (to around 1400 $°C$); step 2, slight temperature decrease due to thermal losses while moving from the preheating device to the converter and waiting for liquid steel tapping; step 3, sudden temperature increase due to tapping of liquid steel into the ladle; step 4, gradual temperature drop due to teeming liquid steel out of the ladle, thermal losses during linings check and, if required, linings repair. Further details on thermal modelling and boundary conditions of each step are given below.

2.3. *Thermal and mechanical modelling*

During the previously described thermal cycle, the temperature distribution of the ladle varies with time and can be obtained by solving the transient form of energy equation given by [15]:

$$\rho C_p \frac{\partial T}{\partial t} - \mathrm{div}\left(k\, \overrightarrow{grad}(T)\right) = 0 \quad (1)$$

Where ρ, C_p, k and T are the density, specific heat, thermal conductivity, and temperature, respectively. Before preheating, the initial temperature (T_i) of all material layers of the ladle is assumed to be the same as ambient temperature. Under this assumption, the initial boundary conditions can be expressed in terms of cylindrical coordinates (R, θ, Z) as:

$$T(R, \theta, Z, t = 0) = T_i = 40^o C \quad (2)$$

During the first step, a natural gas burner is used to heat the inner surface of the ladle from ambient temperature to around $1400^o C$. The time period for this step is around 6.5 hours [8]. The dominant heat transfer mode to the lining surface is radiation with only conduction occurring within the thickness of the different layers. Modelling radiative heat transfer between the burner and lining surface requires solving the full Navier-Stokes equations and energy conservation equations that govern the combustion process. This necessitates long computation time and lies outside the scope of the present work. A simple approach that can reasonably simulate the transient thermal response of the ladle during preheating is to consider convective heat transfer between a heat transfer fluid (HTF) and lining surface. The temperature of the HTF (T_{hf}) is assumed to be $1600\ ^\circ C$. The convective heat flux on the internal surfaces (q_{i1}) of the ladle can be expressed as:

$$q_{i1} = h_{i1}(T_{hf} - T(R, \theta, Z, t)) \quad (3)$$

$$\frac{\partial T_{i1}}{\partial \vec{n}} = h_{i1}(T_{hf} - T(R, \theta, Z, t))\vec{n}$$

Where h_{i1} is the convective heat transfer coefficient during step 1 and $\vec{n}$ is the outward normal to the surface. The radiative and convective thermal losses (q_e) from the outer surfaces of steel shell to the ambient can be written as:

$$q_e = h_e(T_{sh}(R, \theta, Z, t) - T_{amb}) + \epsilon S({T_{sh}}^4(R, \theta, Z, t) - {T_{amb}}^4) \quad (4)$$

Where T_{amb}, ϵ, S, T_{sh} are the ambient temperature ($40\ ^\circ C$), emissivity, Stefan-Boltzmann constant and steel shell outer surface temperature, respectively. This boundary condition has been applied to the external surfaces during the whole steps of the thermal cycle of the ladle.

During step 2, the steel ladle is moved from the heating device to the converter or electric arc furnace and it waits for receiving the liquid steel. The duration of this step may reach $15\ min$. During this period, the inner and outer surfaces of the ladle exchange heat with the environment by convection and radiation mechanisms. The heat losses of the external surface are expressed by Eq. 4, whereas heat losses from the internal surfaces (q_{i2}) are written as:

$$q_{i2} = h_{i2}(T_i(R, \theta, Z, t) - T_{env.}) + \epsilon S(T_i^4(R, \theta, Z, t) - {T_{env.}}^4) \quad (5)$$

With h_{i2}, T_i and $T_{env.}$ denoting heat transfer coefficient during step 2, internal surfaces temperature and environment temperature ($900\ ^\circ C$).

After step 2, liquid steel (with $T_s = 1650\ ^\circ C$) is poured inside the steel ladle leading to a sudden increase in lining temperature (thermal shock). During this step, other processes may occur in parallel (degassing, alloying, etc.) the total duration of this step is assumed to be $2h$. During this period, heat is transferred from the liquid steel to the linings mainly by convection [6]. The convective heat flux on the internal surfaces (q_{i3}) can be expressed as:

$$q_{i3} = h_s\left(T_s - T_i(R, \theta, Z, t)\right) \quad (6)$$

Preprints (www.preprints.org) | NOT PEER-REVIEWED | Posted: 20 March 2020 doi:10.20944/preprints202003.0305.v1

Peer-reviewed version available at Ceramics 2020, 3, 171-188; doi:10.3390/ceramics3020016

Regarding the last step of the thermal cycle (step 4), liquid steel is drained out of the ladle. The ladle's internal and external surfaces temperature decrease gradually due to thermal losses to the ambient. The heat losses during this step are considered similar to those of step 2. It should be noted that the heating and cooling rates during the four steps of the thermal cycle are not constant. Because, according to equation 3, 5 and 6, they are functions of internal surfaces temperature. For example, in the beginning of the first preheating (1st step of 1st thermal cycle) the heating rate is very high as compared to the heating rate at the end of the same step

The thermal model for steel ladle shown in Fig. 1 has been developed using Abaqus software. Then, weak thermomechanical coupling is used. The computed temperature distributions have been used as a thermal load for thermomechanical models. Symmetry boundary conditions have been applied to the symmetric planes of the physical model. The vertical displacement of the bottom of the ladle is assumed to be fixed in the vertical direction (z-direction in Fig. 1). The weight and hydrostatic pressure of liquid steel were neglected as their impact on resulting stresses is very small (around 1 MPa) as compared to the impact of thermal expansion of the bricks (several hundred MPa). The working lining (mortarless refractory masonry) has been replaced by a homogenized equivalent material model that considers joints closure and reopening due to temperature change. Further details about the homogenized equivalent material model, joints closure and reopening criteria are given in section 3.

3. Mechanical homogenization of mortarless masonry structure

In the present work, dry-stack refractory masonry structure shown in Fig. 2 has been studied. Refractory masonry blocks with length (l_b), high (h_b), and width (w_b) are periodically arranged in running bond texture. Joints with thickness (g << l_b, h_b, w_b) are separating the blocks from each other. These joints are present due to surface roughness of the blocks and surface shape defaults. Two categories of joints are defined based on their orientation: bed joints with thickness g_{bed} (in the horizontal direction) and head joints with thickness g_{head} (in the vertical direction). Under thermal or mechanical loading/unloading, these joints can close and reopen leading to a change in the overall thermomechanical response of the refractory masonry structure. The influence of joints closure and reopening on the mechanical behavior should be taken into account when developing accurate numerical models for the analysis and design of dry-stack masonry structures.

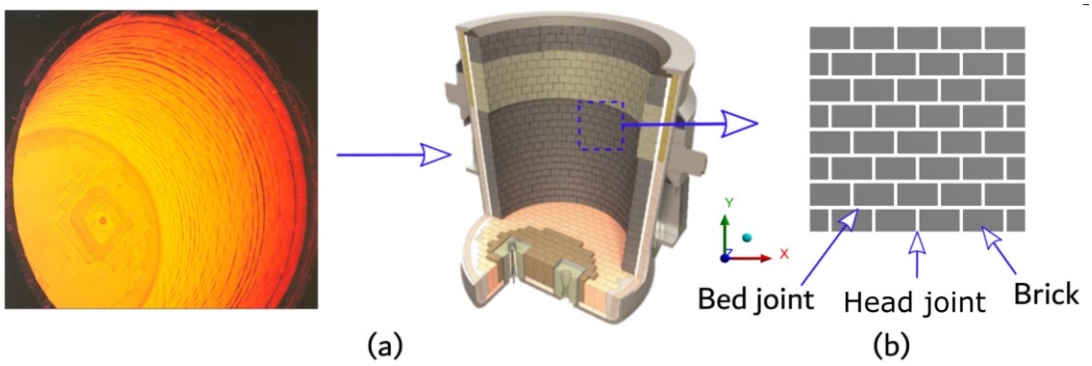

Figure 2. Steel ladle lined with dry-stack refractory masonry: section view (a) and schematic of dry-stack masonry structure (b).

In order to study the influence of joints closure and reopening on the overall mechanical behavior of dry-stack masonry structures, four possible joint patterns have been defined (see Fig. 3). Each joint pattern is associated with a specific state of bed and head joints (open or closed). The four joint patterns are defined as follows [4]:

- Pattern i: bed and head joints are open.
- Pattern ii: bed joints are open, and head joints are closed.
- Pattern iii: bed joints are closed, and head joints are open.

- Pattern iv: bed and head joints are closed.

Each joint pattern represents a different periodic masonry structure with different equivalent elastic behavior. Further details on the determination of equivalent elastic properties of each joint pattern are given in subsection 3.1. Also, joints closure, reopening and transition criteria from one joint pattern to another are described in subsection 3.2.

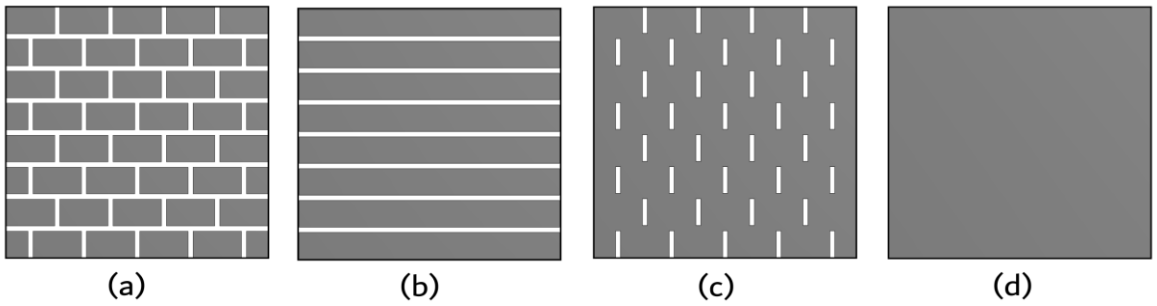

Figure 3. Possible joint patterns of mortarless refractory masonry structure (a) pattern i, (b) pattern ii, (c) pattern iii, and (d) pattern iv.

3.1. Equivalent mechanical behavior of each joint pattern

3.1.1. Joint pattern iv

As previously stated, in case of joint pattern iv, both bed and head joints are closed (see Fig. 3) and, therefore, the macroscopic elastic behavior of the dry-stack masonry structure is similar to that of the constitutive material of the bricks. At high temperature, the constitutive material of the bricks is assumed to undergo small deformations and to exhibit an isotropic linear elasticity. Under these assumptions, the total strain tensor can be decomposed into elastic and thermal strain tensors according to:

$$\bar{\bar{\varepsilon}}^{T} = \bar{\bar{\varepsilon}}^{e} + \bar{\bar{\varepsilon}}^{th} \tag{7}$$

Here $\bar{\bar{\varepsilon}}^{T}$, $\bar{\bar{\varepsilon}}^{e}$, $\bar{\bar{\varepsilon}}^{th}$ are the total, elastic and thermal strains second rank tensor, respectively (in the whole paper, the number of over bars above the symbol indicate the rank of the tensor). The linear elastic strain can be determined using Hooke's law as:

$$\bar{\bar{\varepsilon}}^{e} = \frac{1+\nu}{Y}\bar{\bar{\sigma}} - \frac{\nu}{Y}tr(\bar{\bar{\sigma}})\bar{\bar{I}} \tag{8}$$

With Y, ν denoting the Young's modulus and Poisson's ratio of the constitutive material. $\bar{\bar{\sigma}}$ and $\bar{\bar{I}}$ are the second order stress tensor and second order identity tensor.

3.1.2. Joint pattern iii

In case of joint pattern iii, bed joints are closed whereas head joints are open (see Fig. 3). The presence of open joints leads to a decrease in the effective stiffness of the masonry structures [16]. As a result, the macroscopic elastic behavior of joint pattern iii is different from that of the constitutive material of the bricks and can be determined using finite element-based homogenization technique. To carry out mechanical homogenization of periodic structures (as joint pattern iii), a periodic representative volume element (RVE) with volume (V_Y) has been selected as illustrated in Fig. 4. Then, 3D finite element simulations have been carried out on the RVE to characterize it's homogenized mechanical response and to determine the effective mechanical parameters. The constitutive material has been assumed to exhibit an isotropic linear elasticity and to obey the constitutive equations given in section 3.1.1. Periodic boundary conditions have been used to account for the periodicity of the structure and to ensure that the deformed external surfaces of the RVE are still periodic [17].

Preprints (www.preprints.org) | NOT PEER-REVIEWED | Posted: 20 March 2020 doi:10.20944/preprints202003.0305.v1

Peer-reviewed version available at Ceramics 2020, 3, 171-188; doi:10.3390/ceramics3020016

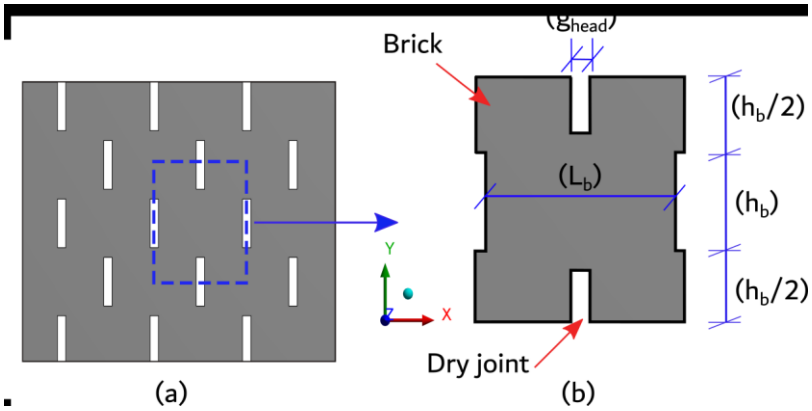

Figure 4. Schematic of periodic mortarless masonry structure in state 3 (a) and unit cell used in the present study (b).

Several finite element simulations of uniaxial tension along x, y and z directions as well as simple shear in xy, xz, and yz planes have been performed. From the simulated combination of uniaxial tensile and simple shear tests, the effective elastic stiffness fourth order tensor ($\bar{\bar{\mathbb{C}}}^e$) of joint pattern iii has been calculated using Hook's law for linear orthotropic elastic materials according to [18]:

$$\bar{\bar{\Sigma}} = \bar{\bar{\mathbb{C}}}^e \, \bar{\bar{\mathrm{E}}}^e \tag{9}$$

With $\bar{\bar{\Sigma}}$ and $\bar{\bar{\mathrm{E}}}^e$ being the second order macroscopic stress and the macroscopic elastic strain tensors, respectively. The homogenized or macroscopic stress can be derived by integrating the local stress ($\bar{\bar{\sigma}}$) over the volume of the unit cell (V_Y) according to Hill's definition as follows [19]:

$$\bar{\bar{\Sigma}} = \langle \bar{\bar{\sigma}} \rangle = \frac{1}{V_Y} \int_{V_Y} \bar{\bar{\sigma}} \, dV \tag{10}$$

The macroscopic strain has been calculated by dividing the average change of displacement on the corners of the RVE by the initial dimensions of the RVE [20]. From the calculated none-zero components of the elastic stiffness matrix $\bar{\bar{\mathbb{C}}}^e$, the effective Youngs modulus (Y), Poisson ratio (ν) and shear modulus (G) have been determined.

3.1.3. Joint Pattern i

As mentioned before, in case of joint pattern i, both bed and head joints are open. One can notice that the mortarless masonry structure is completely disconnected and between the bricks, there are small gaps (see Fig. 3). For computing the effective mechanical properties, one cannot apply finite element-based periodic homogenization technique described previously because the homogenization problem of the cell is not clearly known. But instead, the effective mechanical properties can be assigned directly [4,5]. Due to the presence of open joints, the macroscopic stiffness of the masonry structure in x and y directions is very small. The effective Young's modulus of the masonry is zero in directions x and y ($Y_x = Y_y = 0$, see the coordinate system in Fig. 4). However, the effective Young's modulus in z direction is the same as that of the brick as there are no joints in this direction. The values of the macroscopic elastic constants are reported in table 2. Where Y_b, ν_b and G_b the Youngs modulus, Poisson's ratio and shear modulus of the constitutive material. To facilitate the numerical computations and to avoid numerical singularities, a very small value has been assigned to $Y_x, Y_y, \nu_{xy}, \nu_{xz}, \nu_{yz}$, and G_{xy} instead of zero.

3.1.4. Joint Pattern ii

Preprints (www.preprints.org) | NOT PEER-REVIEWED | Posted: 20 March 2020 doi:10.20944/preprints202003.0305.v1

Peer-reviewed version available at Ceramics 2020, 3, 171-188; doi:10.3390/ceramics3020016

Regarding joint pattern ii, bed joints are open whereas head joints are closed (see Fig. 3). The mortarless masonry structure is composed of an array of separated courses (in y-direction) of bricks. Therefore, the structure has no stiffness in y-direction while it has stiffness in x-direction [4,5]. Similar to joint pattern i, one can define the macroscopic elastic parameters directly. Since bed joints are open, the material stiffness in direction y is very small and Y_y is zero. However, as head joints are closed, Y_x has the same value of the bricks. Also, Young's modulus in z direction has the same value of the brick as there are no joints in this direction. The effective material parameters for the four joint patterns are listed in table 2.

Table 2. Effective mechanical properties of the four joint patterns of mortarless refractory masonry structure.

Parameter	**Pattern** i	**Pattern** ii	**Pattern** iii	**Pattern** iv
Y_x	0	Y_b	Y_h [1]	Y_b [1]
Y_y	0	0	Y_b	Y_b
Y_z	Y_b	Y_b	Y_b	Y_b
ν_{xy}	0	0	ν_h	ν_b
ν_{xz}	0	ν_b	ν_h	ν_b
ν_{yz}	0	0	ν_b	ν_b
G_{xy}	0	0	G_h	G_b
G_{xz}	G_b	G_b	G_h	G_b
G_{yz}	G_b	G_b	G_b	G_b

[1] The subscript h denotes brick homogenization, and the subscript b denotes the brick property.

3.2. Joints closure and reopening criteria

As discussed before, for each joint pattern the equivalent constitutive model has different elastic behavior. During operation, masonry structure is subjected to cyclic thermal heating/cooling. As a result, bed and/ or head joints may close (or reopen). Therefore, the structure may change from one pattern to another leading to a change in the homogenized elastic behavior. This change has been considered by using a suitable joints closure/reopening and pattern transition criterion.

Before loading, the initial joint pattern is usually pattern 1 (bed and head joints are open). Under compression, bed and/ or head joint thickness decreases gradually from the initial value (g_0, from 0.1 to 0.2 mm) till reaching zero and the structure will change to state ii (if head joints close), iii (if bed joints close) or iv (if both bed and head joints close). Bed or head joints are considered to be open or closed based on the instantaneous thickness of joint (g) according to:

$$\begin{array}{lll} \text{Joint open} & \text{if} & g_{bed\ or\ head} > 0 \\ \text{Joint closed} & \text{if} & g_{bed\ or\ head} = 0 \end{array} \quad (11)$$

Since the equivalent material properties are piecewise constant, the displacement increment at every point in the masonry depends linearly on the increment of macroscopic quantities. As a result, one can define the instantaneous thickness of bed and head joints in terms of macroscopic strains according to [4,5]:

$$g_{head} = g_{0,head} + M_X E^T_{xx} \quad (12)$$

$$g_{bed} = g_{0,bed} + M_Y E^T_{yy} \quad (13)$$

Here g_{head} and g_{bed} are the instantaneous thickness of head and bed joint, respectively. $g_{0,head}$ and $g_{0,bed}$ are the initial thickness of head and bed joints, respectively. M_X and M_Y are parameters with the same meaning of localization tensor and they depend on the dimensions of the brick ($M_X = l_b$ and $M_Y = h_b$). E^T_{xx} and E^T_{yy} are the macroscopic total strains (elastic and thermal strains) in x and y directions.

Regarding joints reopening criterion, bed and head joints can reopen if the normal stress to the surface of the joint (bed or head) is higher than zero. This means that a bed joint can reopen if $\sigma_{yy} > 0$ and a head joint can reopen if $\sigma_{xx} > 0$. Since homogeneous stresses are linearly dependent on local

stresses (see Eq. 10), one can rewrite joints reopening criterion in terms of macroscopic stresses using localization tensor ($\sigma_{yy} \rightarrow \Sigma_{yy}$ & $\sigma_{xx} \rightarrow \Sigma_{xx}$). Σ_{XX} and Σ_{YY} can be written in terms of macroscopic strains and non-zero components of macroscopic stiffness matrix as follows [5]:

$$\Sigma_{xx} = \mathrm{D}_{1111} E^{e}_{xx} + \mathrm{D}_{1122} E^{e}_{yy} + \mathrm{D}_{1133} E^{e}_{zz} \tag{14}$$

$$\Sigma_{yy} = \mathrm{D}_{1122} E^{e}_{xx} + \mathrm{D}_{2222} E^{e}_{yy} + \mathrm{D}_{2233} E^{e}_{zz} \tag{15}$$

Here D_{ijkl} is the non-zero components of the elastic stiffness tensor ($\overline{\overline{\mathbb{C}}}^{e}$) determined in previous sections. The transition criteria between pattern i to ii, pattern ii to iii, pattern ii to iv, pattern iii to pattern iv, and vice versa are illustrated in Fig. 5.

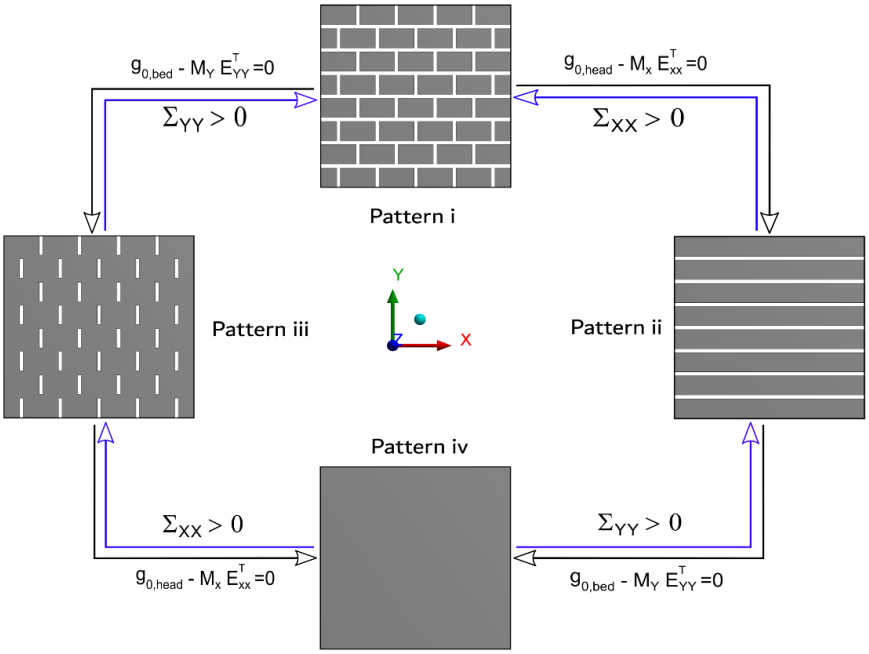

Figure 5. Possible joint patterns of mortarless refractory masonry structure and joints closure/reopening criteria.

4. Results and Discussion

4.1. Validation of the developed homogenized material model

In order to validate the developed homogenized equivalent material model, comparisons between experimental and numerical results of mortarless masonry structure subjected to biaxial compression have been carried out. As can be seen in Figure 6a, the biaxial compression test setup is composed of dry-stack masonry surrounded by four ceramic plates. Two of them are fixed whereas the others can move and are connected to hydraulic pistons. Four linear variable differential transformers (LVDTs) are used to measure the displacement in directions one and tow or "along bed joints and along head joints direction". The biaxial compression test is as follows: first, a preload applied in two directions at the same time and was stopped first in the direction for which the LVDTs detect a displacement, then stopped in the second direction when the LVDTs detect a displacement in the corresponding direction. Finally, loads in both directions have been applied at the same time. displacements, as well as reaction forces of the moving ceramic plates, were recorded. The size of the mortarless masonry is $1100 \times 1100 \times 185\ mm^3$ and the dimensions of the refractory brick are $250 \times 76 \times 185\ mm^3$. Bricks are periodically arranged in a running bond texture and the masonry is made up of 14 courses. The constitutive material of the bricks is magnesia-chrome with Young's modulus $28500\ MPa$ and Poisson's ratio 0.2.

The homogenized material model presented in section 3 has been implemented into Abaqus software using user material subroutine (UMAT) and then used to simulate the biaxial compression test. The four ceramic plates, as well as the support device, have been modeled as rigid plates. Two of them are fixed while displacement boundary conditions have been applied to the other two. The friction between the bricks and the rigid plates and between the bricks and the support device has been considered.

Figure 6b shows a comparison between experimental and numerical results. As can be seen from the figure, both numerical and experimental results are in good agreement. The overall behavior of the masonry is orthotropic and nonlinear due to the gradual closure/reopening of the joints and changing from one joint pattern to another. The reaction forces, in the two directions, increase with the increase of the applied displacement due to the gradual closure of the joints and the increase of material stiffness with joints closure. The displacement in direction 2 is higher than the displacement in direction 1 as the number of joints in direction 2 is higher than in direction 1 (13 bed joints in direction 2 and 8 head joints in direction 1). After unloading, the masonry structure will not return back to the initial configuration and there is always a permanent deformation in both directions. This can be attributed to that the final joint thickness in both directions is less than the initial one.

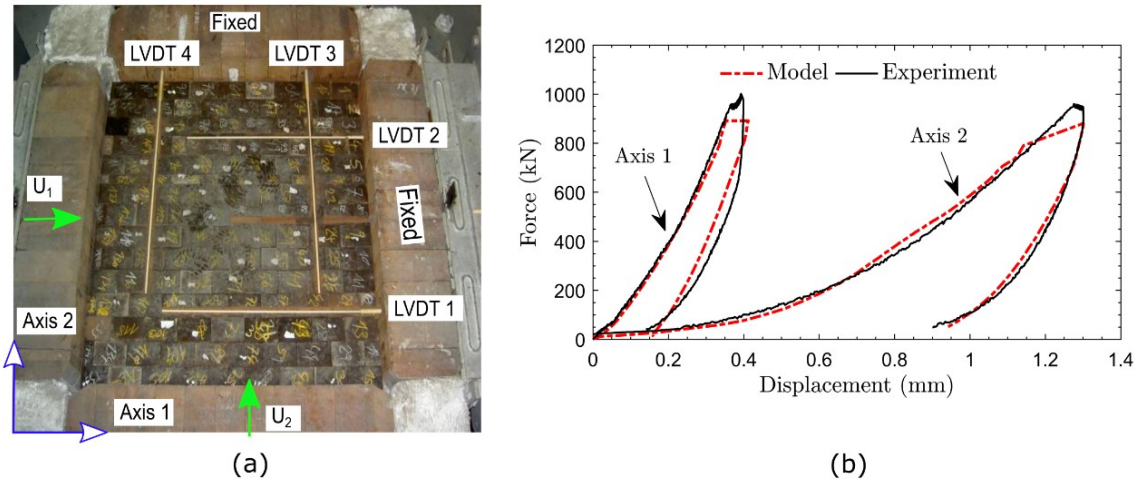

Figure 6. (a) biaxial compression test set up [4] and (b) comparison between experimental and numerical results.

4.2. Temperature distribution

The previous results have shown the capability of the presented homogenized material model to describe the homogenized orthotropic nonlinear elastic behavior of mortarless masonry structures. So, it has been used to analyze the transient thermomechanical response of mortarless refractory masonry structure used in steel ladles. The working lining (mortarless masonry structure) of the steel ladle model shown in Fig. 1 and described in section 2 has been replaced by the developed equivalent material model. Three full production cycles have been modelled to investigate the impact of cyclic temperature change and joint thickness on the thermomechanical behavior of a steel ladle.

Time variations of the temperature of the working lining hot face (surface in contact with liquid steel) and steel shell outer surface (bottom and wall) during the first three complete production cycles are shown in Fig. 7. Temperature distributions at the end of step 1, the end of step 2, the beginning of step 3 and the end of step 4 of the first thermal cycle are presented in Figure 8 (see table 3 for full description of the three simulated thermal cycles). As explained earlier, during the first step (a to b), heat is transferred by forced convection mechanism from a heat transfer fluid at 1600^oC to the working lining (initial temperature is about 40^oC). As a result, the temperature of the working lining increases gradually from room temperature to around 1400^oC. Then, the steel ladle is transported from the heating device to the converter or electric arc furnace while losing heat to the environment by convection and radiation mechanisms (b to c). This leads to a drop in the temperature to around

Preprints (www.preprints.org) | NOT PEER-REVIEWED | Posted: 20 March 2020 doi:10.20944/preprints202003.0305.v1

Peer-reviewed version available at Ceramics 2020, 3, 171-188; doi:10.3390/ceramics3020016

1200^oC. After that (c to d) liquid steel at around 1650^oC is tapped into the ladle resulting in a sudden increase in the temperature. At the end of the thermal cycle (d to e), the working lining temperature decreases gradually. The observed decrease in temperature can be attributed to the teeming of liquid steel and heat losses (by convection and radiation mechanisms) form external and internal surfaces of the ladle to the ambient.

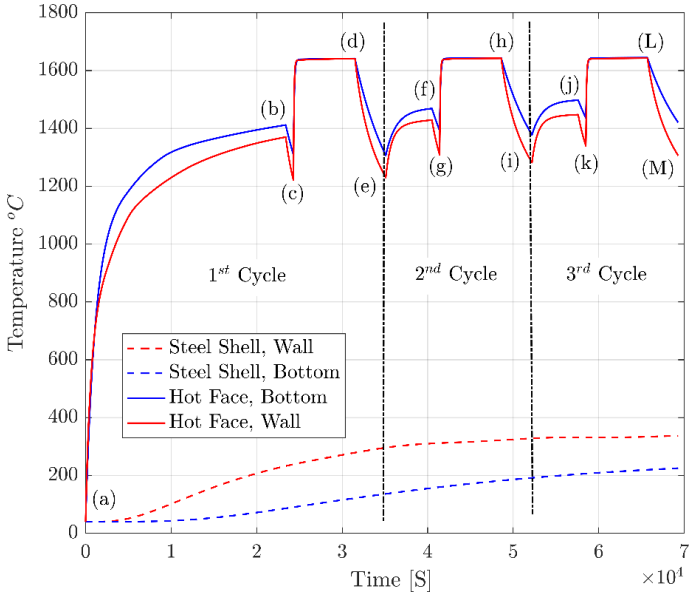

Figure 7. Temperature evolution of inner surface of working lining wall, bottom and outer surface of steel shell during the first three thermal cycles of steel ladle.

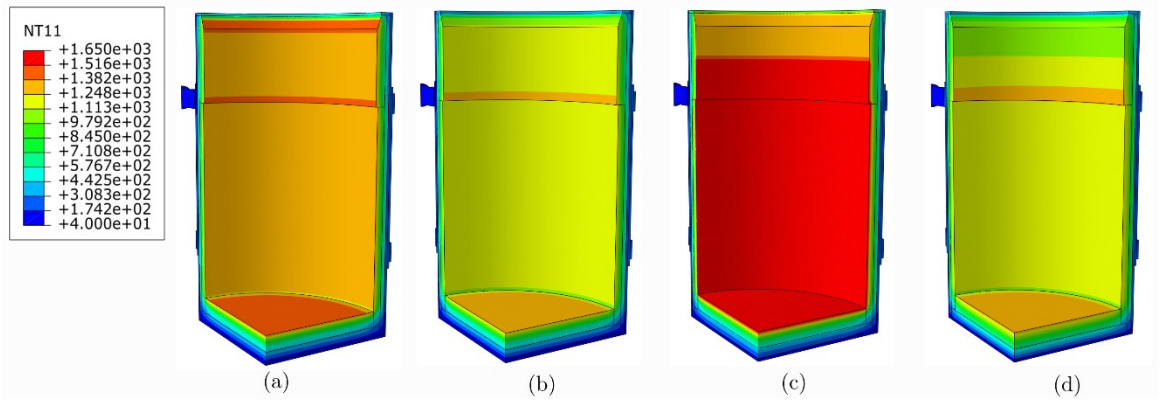

Figure 8. Temperature distributions at the a) end of step 1 (point b in Figure 7), b) end of step 2 (point c in Figure 7), c) end of step 3 (point d in Figure 7), and d) end of step 4 (point e in Figure 7) of the first thermal cycle of the steel ladle.

Table 3. Summary of the three simulated thermal cycles of steel ladle, time period of each step and corresponding points in figure 7.

	First cycle		Second cycle		Third cycle	
	Duration (h)	Corresponding points	Duration (h)	Corresponding points	Duration (h)	Corresponding points
Step 1	6.5	a to b	1.5	e to f	1.5	i to j
Step 2	0.25	b to c	0.25	f to g	0.25	j to k
Step 3	2	c to d	2	g to h	2	k to L
Step 4	1	d to e	1	h to i	1	L to M

Comparisons between temperature gradient through the thickness of steel ladle's wall and bottom at the end of step 2 and end of step 4 of the first three full steel ladle's thermal cycle are shown

Preprints (www.preprints.org) | NOT PEER-REVIEWED | Posted: 20 March 2020 doi:10.20944/preprints202003.0305.v1

Peer-reviewed version available at Ceramics 2020, 3, 171-188; doi:10.3390/ceramics3020016

in Fig. 9. For the second and third thermal cycles, after preheating the temperature of the working lining is slightly higher when compared to the temperature at the end of the first preheating (points f and j as compared to point b in Fig. 7). Similarly, working lining temperature at the end of step 2 (points g and k in Fig. 7) and 4 (points i and m in Fig. 7) of production cycle 2 and 3 is slightly higher than that of first thermal cycle (points c end of step 2 and point e end of step 4 in Fig. 7). This behavior is caused by the overall temperature increase of the ladle after the first preheating cycle (see Fig. 9). It should be mentioned that during the first step of the three simulated production cycles the inner surface temperature of the bottom is slightly higher than that of the wall. Also, the steel shell bottom outer surface temperature is less as compared to that of the steel shell wall. This can be explained by the fact that the thickness of the working and safety lining at the bottom is higher than that at the wall.

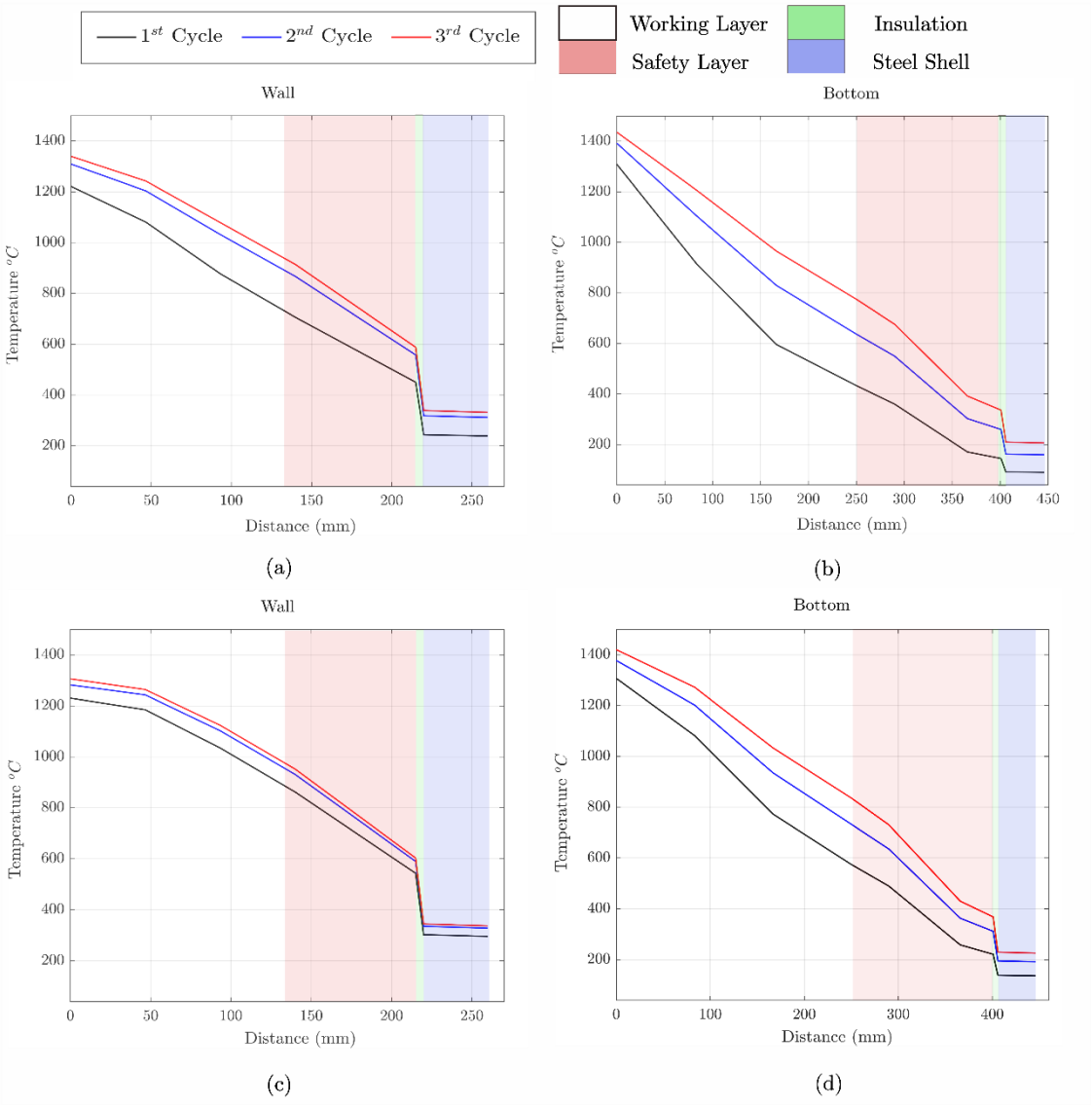

Figure 9. Temperature gradient through the thickness of steel ladle's wall and bottom at a,b) end of step 2 and c,d) end of step 4 of three full ladle's thermal cycle (see table 8 for more details about each step of the thermal cycle). .

4.3. Stress fields

Gradual closure and reopening of joints due to temperature fluctuations during the three thermal cycles are shown in Figure 10. Initially (at time = 0 sec.), bed and head joints are open and, therefore, the working lining (bottom and wall) is in pattern 1. With the increase of temperature,

joints close gradually due to the thermal expansion of the bricks. It has been noticed that joints at the working lining hot surface (internal surface of the ladle) usually close before joints at the cold surface (surface in contact with the permanent lining) (see Fig. 11). At almost 700 sec., all joints in the hot face are closed and remain closed until the end of step 1. At the end of step 2, some joints at the outer top surface of the slag zone (see Fig. 10 f) reopen. This can be attributed to thermal losses, temperature drop of this region and, therefore, change of stress from compression to tension. These open joints close again owing to liquid steel pouring inside the ladle and sudden increase of temperature. Since the temperature drop during step 4 is higher than that during step 2, one can notice that at the end of step 4, more joints are open as compared to the number of open joints at the end of step 2. Therefore, waiting time (after preheating and before liquid steel tapping) is an important issue to consider when defining the time period of each step of the ladle thermal cycle. Long waiting time leads to high energy losses and may results in opening of joints at the wall and the bottom of the steel ladle just before tapping liquid steel in the ladle. Further analysis to investigate the impact of preheating temperature, joint thickness and waiting time on joints reopening is planned to be carried out on the future.

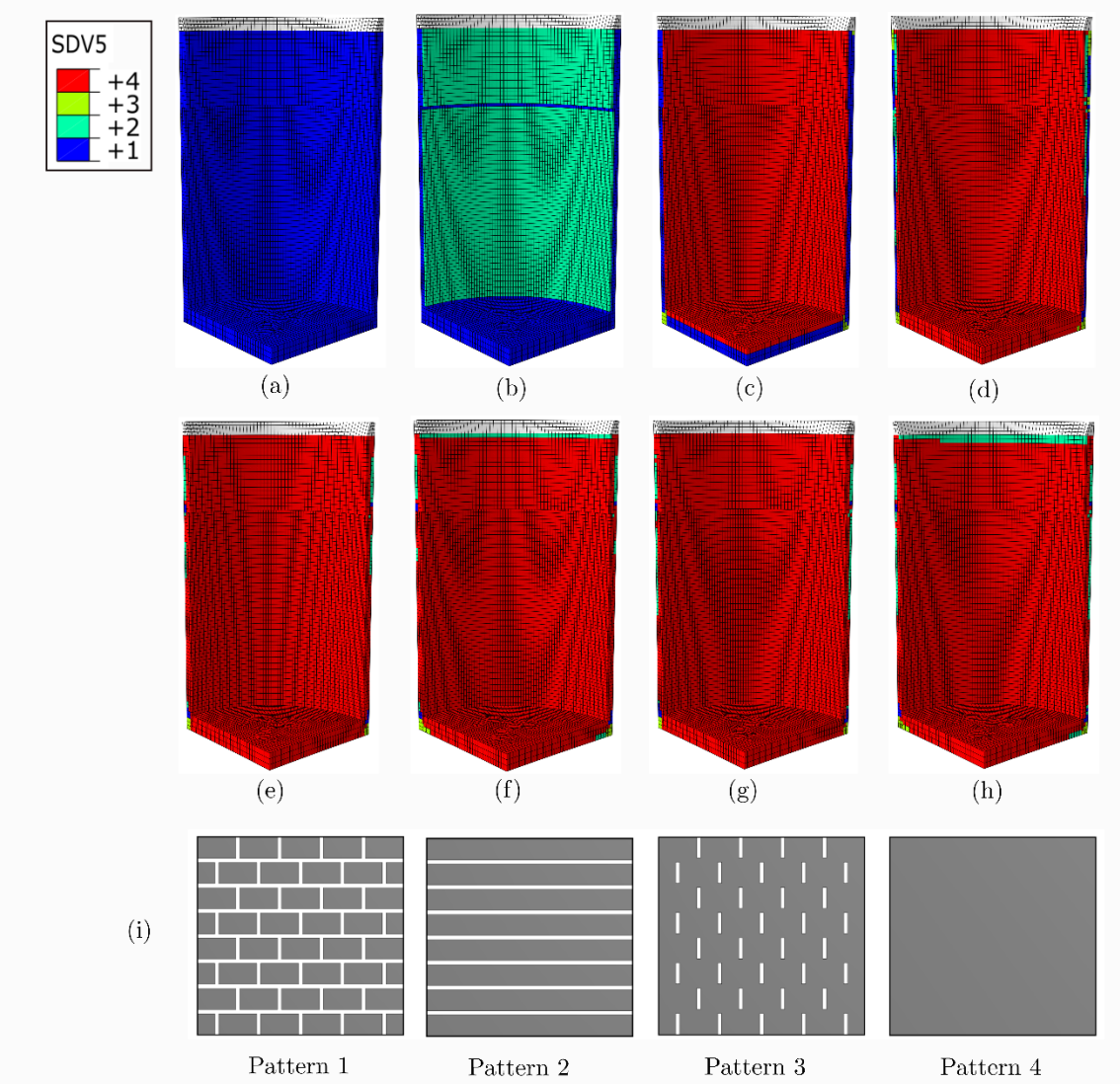

Figure 10. Gradual closure and reopening of joints due to temperature fluctuations during the first heating cycle for joints thickness of 0.1 mm. a) time = 0 s- a on fig. 7, b) time = 460 s , c) time = 675 s d) time = 1825 s - b to d correspond to points after point a and before point b in fig. 7, e) time = 7500 s -b in Fig. 7, f) time = 24300 s – c in Fig. 7, g) time = 24500 s - d in Fig. 7, h) time = 33300 s - e in Fig. 7, and i) schematic of the four joint patterns.

Preprints (www.preprints.org) | NOT PEER-REVIEWED | Posted: 20 March 2020 doi:10.20944/preprints202003.0305.v1

Peer-reviewed version available at Ceramics 2020, 3, 171-188; doi:10.3390/ceramics3020016

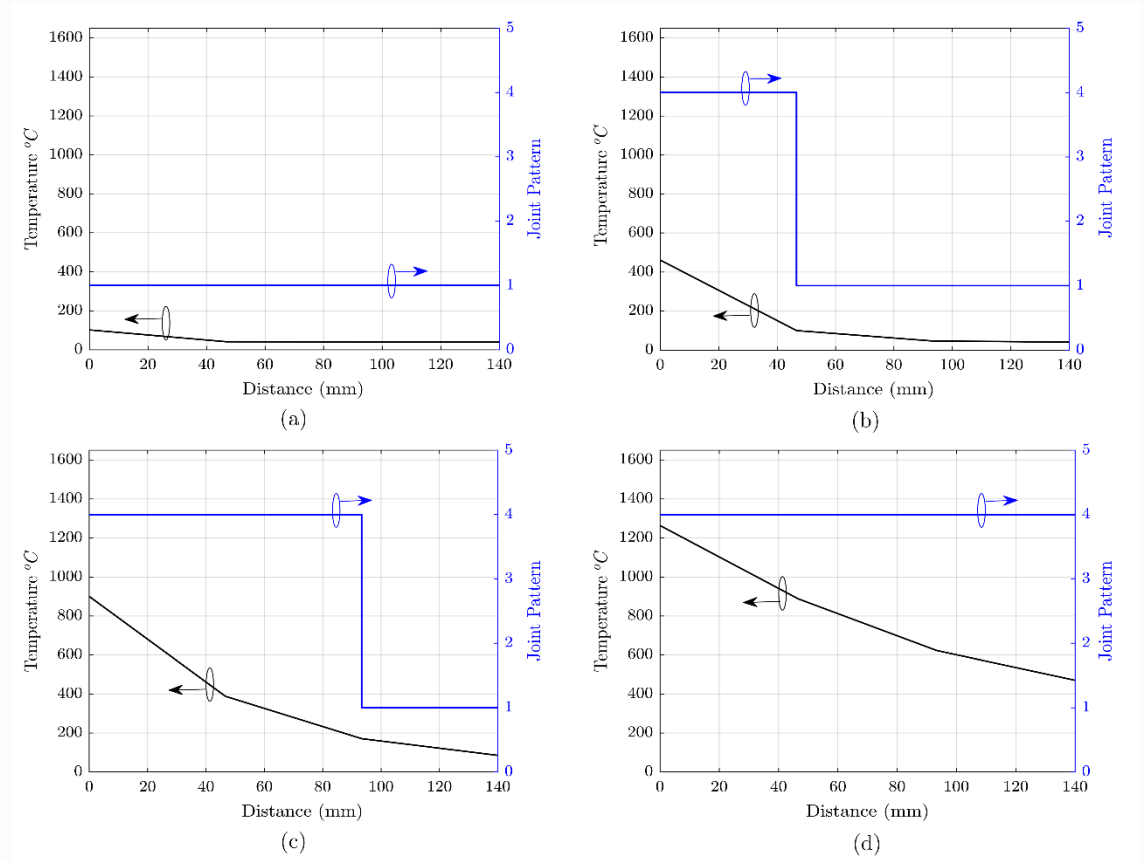

Figure 11. Temperature gradient and joint pattern through the thickness of the working lining (height = 2500 mm) for 0.1 mm bed and head joint thickness at a) time = 50 sec., b) time =675 sec., c) time =1825 sec. and d) time = 7500 sec.

Time variations of the thermal stresses in the hot face of the bottom (center, $R = 0\ mm$) and wall (middle, $H = 2500\ mm$) of the working lining for different values of bed and head joint thickness ($0.1, 0.3$ and $0.5\ mm$) as well as isotropic representation of mortarless masonry (i.e. presence of joints is neglected and properties of the structure are assumed to be the same as those of the bricks) during the first three heating cycle are shown in Figure 12. The brick length and high are taken as $l_b = 160\ mm$ and $h_b = 100\ mm$, and the depth of the bricks is given in Figure 1. In general, it has been observed that resulting thermal stresses increase with the increase of temperature, decrease with the increase of joints thickness and their trends are similar to that of the temperature during the four steps of the ladle thermal cycle. Also, the isotropic assumption of mortarless masonry leads to an overestimation of resulting thermal stresses.

During the first step, thermal stresses increase with the increase of temperature and thermal expansion of the bricks. Then (during step 2), they decrease slightly due to temperature decrease and contraction of the bricks. The maximum value of thermal stresses is reached when liquid steel is tapped in the steel ladle. This is because of the sudden increase in temperature. During step 4, they decrease again with the decrease of temperature. Finally, this trend is repeated. However, for the second and third thermal cycles, resulting thermal stresses are lower as compared to those of the first thermal cycle. This can be attributed to that, at the beginning of second and third thermal cycles, the initial temperature of the steel ladle is much higher as compared to that of the first heat cycling. Therefore, for second and third thermal cycles, temperature gradients history are less as compared to those of the first thermal cycle. Moreover, one can notice that the hot face is under high compressive stresses. This result may be explained by the fact that the temperature of the hot face is higher than the temperature of the other layers and it tends to expand faster than the safety, insulation layers and the steel shell.

Increasing joints thickness leads to a decrease in the resulting thermal stresses in the bottom and the wall of the working lining as well as the steel shell. Increasing joints thickness allows the bricks

Preprints (www.preprints.org) | NOT PEER-REVIEWED | Posted: 20 March 2020 doi:10.20944/preprints202003.0305.v1

Peer-reviewed version available at Ceramics 2020, 3, 171-188; doi:10.3390/ceramics3020016

to expand freely (until closure of joints) resulting in lower values of thermal stresses. After closure of joints, thermal stresses increase at a higher rate. This phenomenon is shown in figure 10-c. In the first 500 seconds, since joints are closing during this period, the values of resulting thermal stresses are very small.

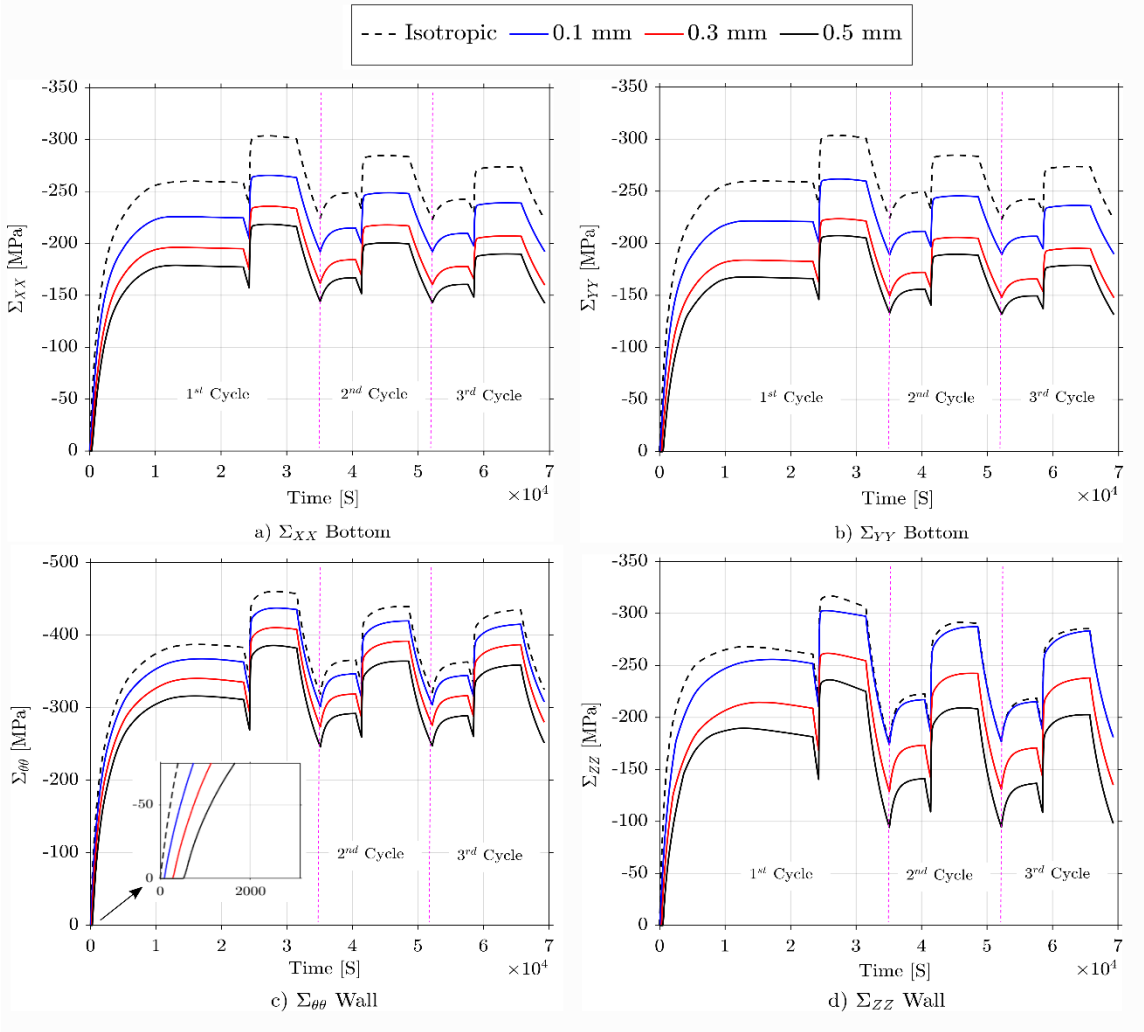

Figure 12. Time variations of the thermal stresses at the bottom surface (a, b) and wall surface of the working lining (c, d) for different values of bed and head joint thickness during the first three thermal cycles of steel ladle.

Time variations of maximum and minimum principal stresses in the hot face, cold face of the working lining as well as Von Mises stresses in the steel shell (bottom and wall) are depicted in Fig. 13. Overall, increasing joints thickness leads to a decrease in maximum, minimum principal stresses in the working lining (hot and cold face) and Von misses stresses in the steel shell. The values of minimum principal stresses in the cold face are less than those of hot face. Because, as discussed earlier, hot face temperature is higher as compared to cold face temperature. At the first 10000 seconds values of maximum principal stresses in the cold face are positive and, as discussed earlier, joints are open (i.e. macroscopic material stiffness in θ and z directions are very small). Therefore, using homogenization technique, lower values of maximum principal stresses are predicted (less than 2 MPa) as compared to the values (around 40 MPa) predicted using isotropic representation of masonry (i.e. presence of joints neglected and material stiffness in θ and z directions are similar to those of the bricks).

Preprints (www.preprints.org) | NOT PEER-REVIEWED | Posted: 20 March 2020 doi:10.20944/preprints202003.0305.v1

Peer-reviewed version available at Ceramics 2020, 3, 171-188; doi:10.3390/ceramics3020016

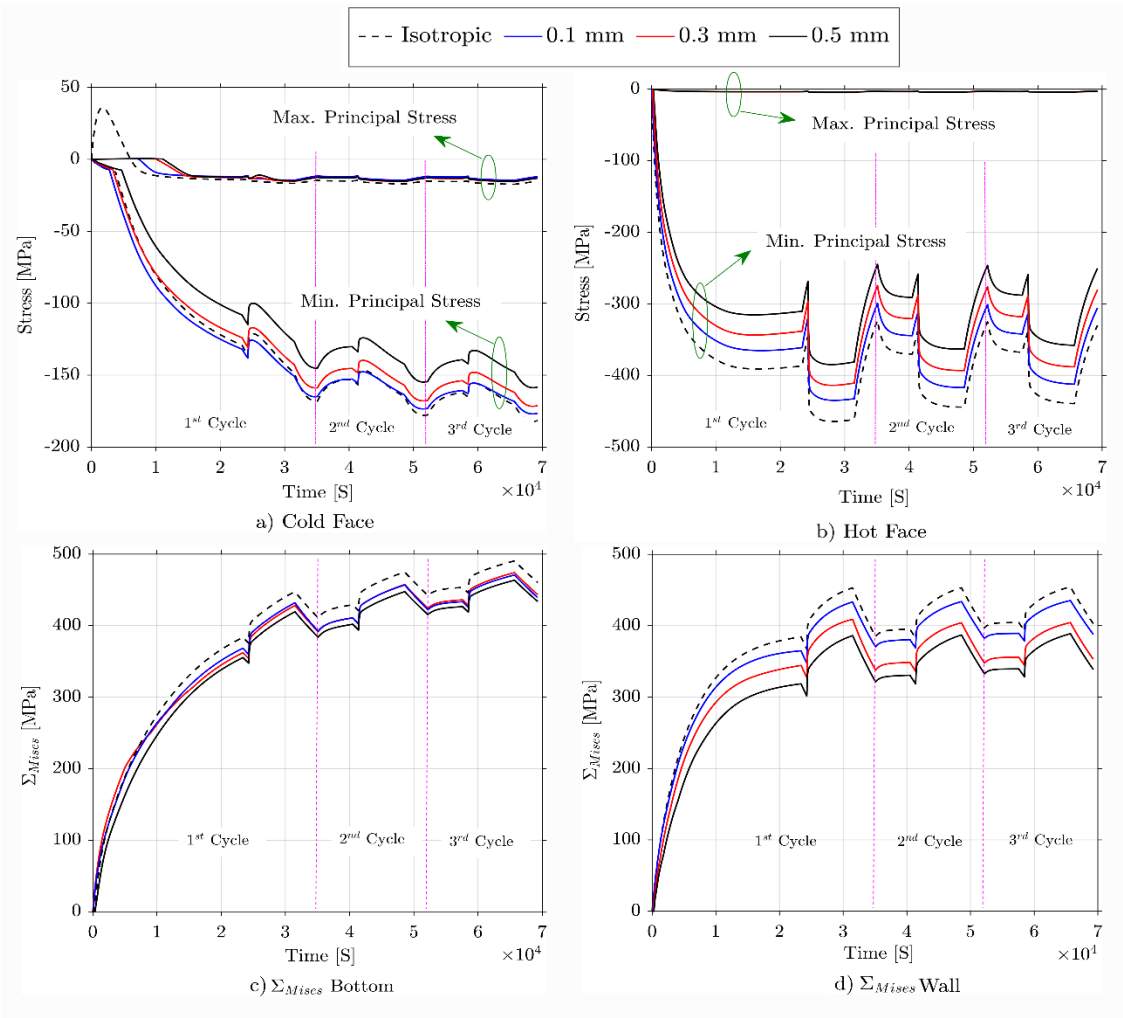

Figure 13. Time variations of maximum and minimum principal stresses in the a) cold face, b) hot face of the working lining as well as Von Mises stresses in the steel shell c) bottom and d) wall.

5. Conclusion and perspective

In the present work, three-dimensional coupled sequential thermomechanical analysis of steel ladle has been carried out. The working lining and the bottom of the ladle have been replaced by an equivalent material model that takes into account the joints closure and reopening due to cyclic thermal or mechanical loading /unloading. The temperature distribution of the steel ladle has been computed and used as a thermal load for the thermomechanical analysis. The thermomechanical model enables the visualization of gradual joints closure and reopening during the complete thermal cycle of the ladle. The impact of joint thickness on the resulting thermal stresses has been studied. The following conclusions can be drawn:

- With the increase of temperature, dry joints close gradually due to the thermal expansion of the bricks. Joints at the working lining hot surface close faster than joints at the cold surface.
- Temperature drop during waiting time results in opening of some joints at the outer top surface of the slag zone. Moreover, waiting time is an important issue to consider when defining the time period of each step of the ladle thermal cycle. Long waiting time leads to high energy losses and may result in opening of joints at the wall and the bottom of the steel ladle just before tapping liquid steel in the ladle.
- Resulting thermal stresses in the hot face increase with the increase of temperature and their trends are similar to that of the temperature during the four steps of the thermal ladle heating cycle. However, during second and third thermal cycle, values of resulting

thermal stresses are less as compared to those of the first thermal cycle. As the maximum stress is proportional to the difference between the local maximum temperature and the average temperature in the thickness. So, after the second and third cycles, the average temperature is higher and then the stress decrease

- The working lining hot face is under high compressive stresses, on the other hand, the cold face is under tensile stresses when joints are open during the first 10000 seconds of step 1 of the first thermal cycle (1st preheating) and heat losses steps (step 2 and 4 of the thermal cycle).
- Increasing joints thickness leads to a decrease in the resulting thermal stresses in the bottom and the wall of the working lining as well as in the steel shell.

In perspective, this study could be exploited as the first step in nonlinear multi-scale thermomechanical analysis of refractory masonry structures. Further parametric studies to investigate maximum possible joints thickness wherein preheating will not allow enough closure to contain liquid steel are also planned to be carried out. Also, further developments of the equivalent material model to consider creep of mortarless refractory masonry structure will allow better prediction of thermal stress levels, design and optimization of thermally and mechanically efficient steel ladles. Work on this line is ongoing at LaMé laboratory, University of Orléans.

Author Contributions: "conceptualization, M.A, A.G and T.S; methodology, M.A, A.G. and T.S; software, M.A, and T.S; validation, M.A; formal analysis, M.A; investigation, M.A; resources, M.A; writing—original draft preparation, M.A; writing—review and editing, A.G , T.S and E.B; visualization, M.A; supervision, T.S, A.G and E.B; project administration, A.G; funding acquisition, A.G and E.B"

Funding: This work was supported by the funding scheme of the European Commission, Marie Skłodowska Curie Actions Innovative Training Networks in the frame of the project ATHOR - Advanced Thermomechanical mOdelling of Refractory linings 764987 Grant

Acknowledgments: The authors are grateful to the Centre de Calcul Scientifique en région Centre Val de Loire (France) for the computation time and technical support.

Conflicts of Interest: The authors declare no conflict of interest.

References

1. Blond, E.; Schmitt, N.; Hild, F.; Blumenfeld, P.; Poirier, J. Effect of Slag Impregnation on Thermal Degradations in Refractories. *Journal of the American Ceramic Society* **2007**, *90*, 154–162.
2. Andreev, K.; Sinnema, S.; Rekik, A.; Allaoui, S.; Blond, E.; Gasser, A. Compressive behaviour of dry joints in refractory ceramic masonry. *Construction and Building Materials* **2012**, *34*, 402–408.
3. Allaoui, S.; Rekik, A.; Gasser, A.; Blond, E.; Andreev, K. Digital Image Correlation measurements of mortarless joint closure in refractory masonries. *Construction and Building Materials* **2018**, *162*, 334–344.
4. Nguyen, T.M.H.; Blond, E.; Gasser, A.; Prietl, T. Mechanical homogenisation of masonry wall without mortar. *European Journal of Mechanics - A/Solids* **2009**, *28*, 535–544.
5. Ali, M.; Sayet, T.; Gasser, A.; Blond, E. Thermomechanical Modelling of Refractory Mortarless Masonry Wall Subjected to Biaxial Compression. In Proceedings of the Unified International Technical Conference of Refractories; Yokohama, Japan, 2019.
6. Xia, J.L.; Ahokainen, T. Transient flow and heat transfer in a steelmaking ladle during the holding period. *Metallurgical and Materials Transactions B* **2001**, *32*, 733–741.
7. Glaser, B.; Görnerup, M.; Sichen, D. Fluid Flow and Heat Transfer in the Ladle during Teeming. *steel research international* **2011**, *82*, 827–835.
8. Santos, M.F.; Moreira, M.H.; Campos, M.G.G.; Pelissari, P.I.B.G.B.; Angélico, R.A.; Sako, E.Y.; Sinnema, S.; Pandolfelli, V.C. Enhanced numerical tool to evaluate steel ladle thermal losses. *Ceramics International* **2018**, *44*, 12831–12840.

9. Yilmaz, S. Thermomechanical Modelling for Refractory Lining of a Steel Ladle Lifted by Crane. *Steel Research International* **2003**, *74*, 485–490.
10. Hou, A.; Jin, S.; Harmuth, H.; Gruber, D. A Method for Steel Ladle Lining Optimization Applying Thermomechanical Modeling and Taguchi Approaches. *JOM* **2018**, *70*, 2449–2456.
11. Gasser, A.; Chen, L.; Genty, F.; Daniel, J.L.; Blond, E.; Andreev, K.; Sinnema, S. Influence of different masonry designs of bottom linings. In Proceedings of the Unified International Technical Conference of Refractories; Victoria, Canada, 2013.
12. Shakhtin, D.M.; Pechenezhskii, V.I.; Karaulov, A.G.; Kvasman, N.M.; Kravchenko, V.P.; Kabakova, I.I.; Ustichenko, V.A.; Kalita, G.E.; Shcherbenko, G.N.; Yakobchuk, L.M. Thermal conductivity of corundum, high-alumina, magnesia, zirconium, and chromate refractories in the 400–1800 °C range. *Refractories* **1982**, *23*, 223–227.
13. Nemets, I.I.; Nestertsov, A.I.; Zagoskin, V.T.; Vysotskii, D.A.; Stavrovskii, G.I.; Chekhovskoi, V.Ya. The thermal conductivity of periclase and periclase — Spinel refractories. *Refractories* **1975**, *16*, 178–180.
14. Díaz, L.A.; Torrecillas, R.; Simonin, F.; Fantozzi, G. Room temperature mechanical properties of high alumina refractory castables with spinel, periclase and dolomite additions. *Journal of the European Ceramic Society* **2008**, *28*, 2853–2858.
15. Pletcher, R.H.; Tannehill, J.C.; Anderson, D. *Computational fluid mechanics and heat transfer*; CRC Press, 2012;
16. Rekik, A.; Nguyen, T.T.N.; Gasser, A. Multi-level modeling of viscoelastic microcracked masonry. *International Journal of Solids and Structures* **2016**, *81*, 63–83.
17. Xia, Z.; Zhang, Y.; Ellyin, F. A unified periodical boundary conditions for representative volume elements of composites and applications. *International Journal of Solids and Structures* **2003**, *40*, 1907–1921.
18. Iltchev, A.; Marcadon, V.; Kruch, S.; Forest, S. Computational homogenisation of periodic cellular materials: Application to structural modelling. *International Journal of Mechanical Sciences* **2015**, *93*, 240–255.
19. Hill, R. The essential structure of constitutive laws for metal composites and polycrystals. *Journal of the Mechanics and Physics of Solids* **1967**, *15*, 79–95.
20. Michel, J.C.; Moulinec, H.; Suquet, P. Effective properties of composite materials with periodic microstructure: a computational approach. *Computer Methods in Applied Mechanics and Engineering* **1999**, *172*, 109–143.